

Single-layer Janus black arsenic-phosphorus (b-AsP): Optical dichroism, anisotropic vibrational, thermal, and elastic properties

L. L. Li,^{1,2,*} C. Bacaksiz,² M. Nakhaee,^{2,3} R. Pentcheva,¹ F. M. Peeters,² and M. Yagmurcukardes^{2,†}

¹*Department of Physics and Center for Nanointegration, University of Duisburg-Essen, Lotharstrasse 1, 47057 Duisburg, Germany*

²*Department of Physics, University of Antwerp, Groenenborgerlaan 171, 2020 Antwerpen, Belgium*

³*School of Physics, University of Damghan, P.O. Box 36716-41167, Damghan, Iran*



(Received 11 November 2019; revised manuscript received 29 January 2020; accepted 4 March 2020; published 8 April 2020)

By using density functional theory (DFT) calculations, we predict a puckered, dynamically stable Janus single-layer black arsenic-phosphorus (b-AsP), which is composed of two different atomic sublayers, arsenic and phosphorus atoms. The calculated phonon spectrum reveals that Janus single-layer b-AsP is dynamically stable with either pure or coupled optical phonon branches arising from As and P atoms. The calculated Raman spectrum indicates that due to the relatively strong P-P bonds, As atoms have no contribution to the high-frequency optical vibrations. In addition, the orientation-dependent isovolume heat capacity reveals anisotropic contributions of LA and TA phonon branches to the low-temperature thermal properties. Unlike pristine single layers of b-As and b-P, Janus single-layer b-AsP exhibits additional out-of-plane asymmetry which leads to important consequences for its electronic, optical, and elastic properties. In contrast to single-layer b-As, Janus single-layer b-AsP is found to possess a direct band gap dominated by the P atoms. Moreover, real and imaginary parts of the dynamical dielectric function, including excitonic effects, reveal the highly anisotropic optical feature of the Janus single-layer. A tight-binding (TB) model is also presented for Janus single-layer b-AsP, and it is shown that, with up to seven nearest hoppings, the TB model reproduces well the DFT band structure in the low-energy region around the band gap. This TB model can be used in combination with the Green's function approach to study, e.g., quantum transport in finite systems based on Janus single-layer b-AsP. Furthermore, the linear-elastic properties of Janus single-layer b-AsP are investigated, and the orientation-dependent in-plane stiffness and Poisson ratio are calculated. It is found that the Janus single layer exhibits strong in-plane anisotropy in its Poisson ratio much larger than that of single-layer b-P. This Janus single layer is relevant for promising applications in optical dichroism and anisotropic nanoelasticity.

DOI: [10.1103/PhysRevB.101.134102](https://doi.org/10.1103/PhysRevB.101.134102)

I. INTRODUCTION

Two-dimensional (2D) single-layer materials have gained a lot of interest in the field of condensed-matter physics and materials science [1]. Graphene [2], a single layer of carbon atoms arranged in a honeycomb lattice, exhibits various fascinating properties due to its Dirac fermions [3]. Inspired by the successful isolation of graphene, a great number of 2D single-layer materials were successfully fabricated, including silicene [4], germanene [5], and stanene [6]. Two-dimensional transition-metal dichalcogenides have also drawn much attention in the context of optoelectronics, spintronics, and valleytronics utilizing the combination of strong spin-orbit coupling and intrinsic valley degrees of freedom [7–11].

Recently, in-plane anisotropic materials have become the focus of interest due to their direction-dependent electronic and optical properties. Single-layer black phosphorus (b-P) was successfully exfoliated from its bulk form and has become an important member of the anisotropic 2D

family [12]. Monolayer b-P was demonstrated to have the combined properties of direct band gap and high carrier mobility, which makes it well suited for practical electronic and optoelectronic applications in, e.g., field-effect transistors and solar cells [13–17]. Very recently, a cousin of b-P, so-called black arsenic (b-As), was thinned down to its 2D limit and was found to be another strongly in-plane anisotropic material [18]. Following its successful synthesis, the structural, mechanical, and vibrational properties of single-layer b-As were investigated by means of density functional theory (DFT) calculations. Its dynamical stability was confirmed, indicating that it can be realized as a freestanding single layer [19,20].

In addition to extensive research efforts on pristine 2D materials, recent advances in experimental techniques have allowed researchers to combine properties of MoS₂ and MoSe₂ in a single polar material, namely, Janus MoSSe [21,22]. Following the experimental realization, the energetic feasibility of other possible Janus single-layer structures of different 2D materials has been investigated theoretically [23–25]. On the other hand, alloyed black arsenic-phosphorus (b-AsP) structures with different compositions (b-As_xP_{1-x}) were recently experimentally synthesized [26–28]. Moreover, single layers

*longlong.li@uni-due.de

†mehmetyagmurcukardes.edu@gmail.com

of alloyed b-AsP were proposed, and their functionalization by different adatoms was theoretically investigated [29].

Motivated by the above experimental and theoretical studies [21–24,26–29], here, we predict a dynamically stable Janus single-layer b-AsP which has a puckered lattice consisting of two different atomic sublayers. This Janus single-layer could, in principle, be experimentally synthesized by using the combination of Janus engineering and alloying methods. Notably, the already synthesized and predicted structures of b-AsP (including equal amounts of As and P) were recently announced to be in alloy form; however, they are totally different from the Janus structures investigated in this paper. The calculated phonon spectrum reveals that Janus single-layer b-AsP is dynamically stable with either pure or coupled optical phonon branches arising from As and P atoms. The calculated Raman spectrum indicates that due to the relatively strong P-P bonds, As atoms have no contribution to the high-frequency optical vibrations. In addition, the orientation-dependent iso-volume heat capacity reveals anisotropic contributions of LA and TA phonon branches to the low-temperature thermal properties. Unlike pristine single layers of b-As and b-P, the Janus single layer of b-AsP exhibits additional out-of-plane asymmetry which leads to important consequences for its electronic, optical, and elastic properties. In contrast to single-layer b-As, Janus single-layer b-AsP is found to possess a direct band gap semiconducting behavior whose band edges are dominated by P atoms. Moreover, the real and imaginary parts of the frequency-dependent dielectric function, including excitonic effects, reveal the highly anisotropic optical feature of the Janus single layer. A tight-binding (TB) model is presented for Janus single-layer b-AsP, and it is shown that, with up to seven nearest hoppings, the TB model reproduces well the DFT band structure in the low-energy region around the band gap. This TB model can be used in combination with, e.g., the Green's function approach to study, e.g., quantum transport in finite systems based on Janus single-layer b-AsP. Furthermore, the linear-elastic properties of Janus single-layer b-AsP are investigated, and the orientation-dependent in-plane stiffness and Poisson ratio are calculated. It is found that the Janus single layer exhibits strong in-plane anisotropy in its Poisson ratio much larger than that of single-layer b-P. The strong anisotropy of Janus single-layer b-AsP shown by its optical and elastic properties suggests that this 2D material is relevant for promising applications in optical dichroism and anisotropic nanoelasticity.

II. COMPUTATIONAL METHODOLOGY

The first-principles calculations were carried out within the framework of DFT as implemented in the Vienna Ab initio Simulation Package (VASP) [30]. The generalized gradient approximation (GGA) within the Perdew-Burke-Ernzerhof [31] formalism and the Heyd-Scuseria-Ernzerhof (HSE06) [32] hybrid functional were employed to account for the exchange-correlation potential. The projector augmented wave method and a plane-wave basis with an energy cutoff of 500 eV were used in the calculations. For geometry optimization the Brillouin-zone integration was performed on a $10 \times 14 \times 1$ Γ -centered k -point mesh obtained within the Monkhorst-Pack scheme. The convergence criterion for the electronic

self-consistent calculation was set to 10^{-6} eV for the total energy. For 2D single-layer calculations, a vacuum layer of 20 Å was used to prevent spurious (unphysical) interaction between two periodic layers. By using the conjugate gradient method, atomic positions and lattice constants were optimized until the Hellmann-Feynman forces were less than 10^{-5} eV/Å and pressure on the unit cell was minimized to values less than 1 kBar. For the electronic-band structure calculations spin-orbit coupling (SOC) was included on top of GGA and HSE06. The value of the mixing parameter which specifies the fraction of exact exchange in the HSE06 hybrid functional calculations was taken to be 0.25. Moreover, the Gaussian smearing factor was chosen to be 0.05 eV in the DFT calculations.

Phonon dispersion curves were calculated by using the small-displacement method as implemented in the PHON code [33]. The phonon frequencies and the corresponding off-resonant Raman activities were calculated at the Γ point of the Brillouin zone (BZ) using the small-displacement method. Each atom in the primitive unit cell was initially distorted by 0.01 Å, and the corresponding dynamical matrix was constructed. Then, the vibrational modes were determined by a direct diagonalization of the dynamical matrix. The corresponding Raman activity of each phonon mode was obtained from the derivative of the macroscopic dielectric tensor by using the finite-difference method [34,35].

In order to obtain the optical properties, we calculated the frequency-dependent dielectric function including excitonic effects by solving the Bethe-Salpeter equation (BSE) on top of the quasiparticle energy states determined by using the GW approximation. The energy cutoffs for the wave functions and for the response functions was set to 500 and 200 eV, respectively. Since the number of empty bands influences significantly the relative position of the quasiparticle energy states, we used 200 empty bands for the GW and BSE calculations to make the quasiparticle energies and exciton binding energies reasonably converge. The six highest occupied valence bands and the six lowest unoccupied conduction bands were included as a basis in the BSE calculations for the excitonic states. Since the GW calculations require a sufficiently large vacuum region, a vacuum region of at least 15 Å was inserted to avoid spurious interaction between the periodic images.

III. STRUCTURAL AND VIBRATIONAL PROPERTIES

In their ground-state phases, both b-As and b-P exhibit a puckered honeycomb structure consisting of two parallel layers of either As or P atoms. Regarding the formation methodology of the recently synthesized Janus MoSSe crystal, the Janus single-layer form of b-AsP is constructed such that the top layer of the structure is composed of As atoms while the bottom layer contains only P atoms [see Fig. 1(a)]. This type of AsP structure is entirely different from that of the already investigated $\text{As}_{0.5}\text{P}_{0.5}$ alloy crystal [29]. The optimized in-plane lattice parameters are calculated to be $a = 4.72$ Å and $b = 3.47$ Å. Compared to those for single layers of b-As (4.71 and 3.67 Å) and b-P (4.57 and 3.31 Å), a dominant uniaxial strain occurs along the armchair (AC) direction on the P surface, while an approximately equal amount of strain is induced at both surfaces along the zigzag

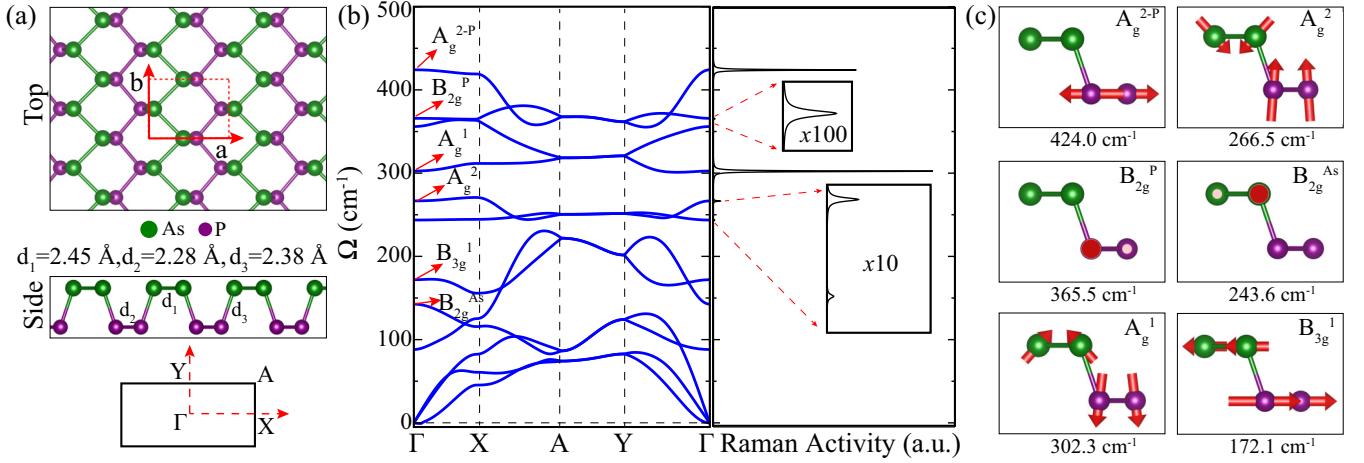


FIG. 1. Optimized single-layer Janus b-AsP crystal: (a) top and side views with the corresponding bond lengths and Brillouin zone, (b) phonon band dispersion and the corresponding Raman activity, and (c) the vibrational motion of the individual atoms of the phonon modes indicated in (b).

(ZZ) direction. In addition, the anisotropy ratio between the two lattice parameters ($a/b = 1.36$ for Janus) is very close to that of single-layer b-P (1.38) but larger than that of b-As (1.28), suggesting larger anisotropy along two directions. The three different bond lengths, d_1 (As-As), d_2 (P-P), and d_3 (As-P), are found to be 2.45, 2.28, and 2.38 Å, respectively, as listed in Table I.

The dynamical stability of Janus single-layer b-AsP is examined by calculating its phonon spectrum. We find that the Janus structure is free from any imaginary frequencies through the whole BZ, indicating its dynamical stability. The Janus single-layer b-AsP exhibits 12 phonon branches, three of which are acoustical, LA, TA, and ZA, while the others are optical branches which are labeled as shown in Fig. 1(b). The vibrational motion of six optical phonon modes which arise from the vibrations of As atoms, P atoms, or their coupled motions is shown in Fig. 1(c). The phonon mode B_{3g}^1 arises from the in-plane shear vibration of As and P layers against each other along the AC direction with a frequency of 172.1 cm^{-1} . Its Raman activity is found to be the smallest (10^4 times smaller than the most prominent peak). The B_{2g}^{As} phonon mode with frequency 243.6 cm^{-1} is attributed to the in-plane opposite vibration of As atoms along the ZZ direction. A_g^2 has a frequency of 266.5 cm^{-1} and shows a coupled breathinglike motion of the As and P layers with a Raman activity which is 30 times smaller than that of the prominent

peak. Another coupled phonon mode, A_g^1 , corresponds to a mostly out of plane vibration of As and P layers against each other and has a frequency of 302.3 cm^{-1} . Our results reveal that the most prominent Raman active mode is A_g^1 , which should be observable experimentally. Another low-Raman activity phonon mode, B_{2g}^P , is attributed to the opposite in-plane vibration of the P atoms along the ZZ direction and has a frequency of 365.5 cm^{-1} . The highest-frequency Raman active mode is 424.0 cm^{-1} , and it is attributed to the in-plane vibration of P atoms along the AC direction against each other. It is evident that the Janus single-layer exhibits combined vibrational properties of both b-As and b-P single layers.

One important property of a material is its thermal behaviors, which is important for applications in nanoscale devices at finite temperatures. Based on the phonon band dispersions, the thermal properties of b-P, b-As, and b-AsP are investigated in terms of their orientation-dependent isovolume heat capacity as a function of temperature. As shown in Fig. 2, all three heat capacity curves rapidly increase in the low-temperature regime and asymptotically approach the classical limit of $3Nk_B$ where N and k_B denote the number of atoms and the Boltzmann constant, respectively.

It was previously reported that the low-temperature behavior of the heat capacity of the 2D crystals is determined by the phonon modes [36,37]. Considering the phonon band structures of b-P, b-As, and b-AsP, the low-temperature thermal excitations take place in acoustic phonon branches, and consequently, the heat capacity is governed by the acoustic phonons. In addition, for 2D crystals, while the heat capacity scales with temperature as $C_v \sim T^{2n-1}$, the phonons contributing to the thermal properties have a dispersive behavior given as $\omega \sim \gamma q^n$. According to our calculations, the heat capacities of b-P, b-As, and b-AsP at low temperatures (shown in the inset in Fig. 2) scale with temperature as $T^{1.89}$, $T^{2.08}$, and $T^{1.92}$, respectively. Considering the relation given above, $n \sim 1$ for the phonon modes contributing to the heat capacity. From the phonon band structures, we calculate the power n which corresponds to the relation between the frequency ω and wave vector q of the three acoustic phonon modes around

TABLE I. For the single layers of b-As, b-P, and Janus b-AsP, optimized lattice parameters a and b , the bond length between constituent atoms $d_{X/Y}$, energy band gap calculated within HSE on top of GGA+SOC $E_{\text{gap}}^{\text{HSE}}$, and the valence and conduction band edges in the BZ.

	a (Å)	b (Å)	$d_{\text{As/As}}$ (Å)	$d_{\text{P/P}}$ (Å)	$d_{\text{As/P}}$ (Å)	$E_{\text{gap}}^{\text{HSE}}$ (eV)	VB/CB
b-As	4.72	3.47	2.48/2.50			1.29	X- Γ / Γ
b-P	4.57	3.31		2.22/2.26		1.55	Γ / Γ
b-AsP	4.71	3.67	2.45	2.28	2.38	1.49	Γ / Γ

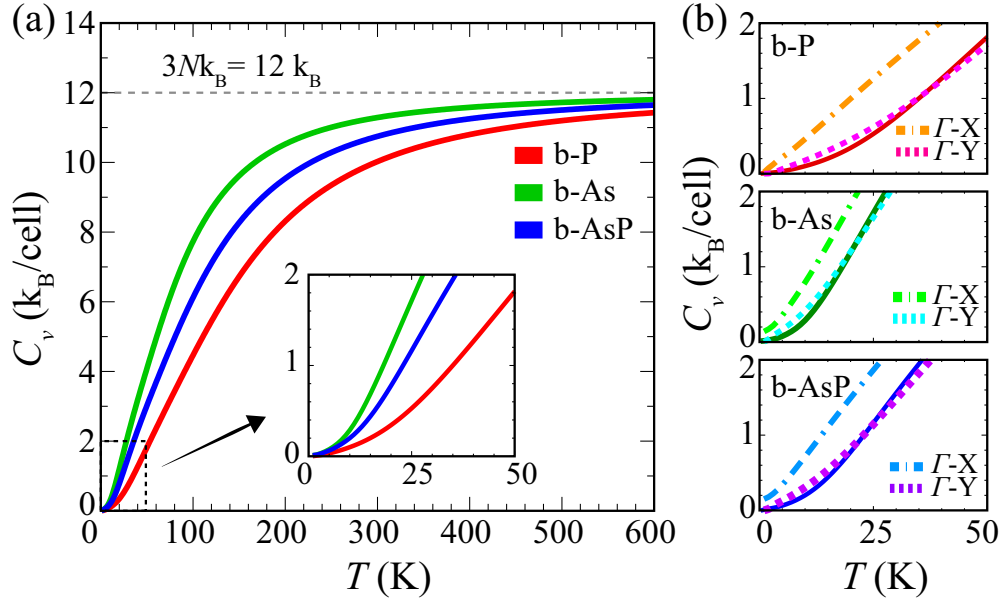


FIG. 2. (a) Isovolume heat capacity of single-layer b-P, b-As, and b-AsP. The quadraticlike behaviors of the curves at low temperature are shown in the inset. (b) The directional contributions of the different phonon branches to the heat capacity.

Γ (i.e., $\omega \sim \gamma q^n$) in order to find the contributions to the heat capacity. For b-P, it is found that $n_{ZA} = 1.5$, $n_{LA} = 1.00$, and $n_{TA} = 0.99$, which means that the main contributions to the heat capacity arise from the in-plane acoustic (LA and TA) modes for b-P. For b-As and b-AsP, we obtain $n_{ZA} = 2.16$, $n_{LA} = 0.99$, $n_{TA} = 0.99$ and $n_{ZA} = 2.27$, $n_{LA} = 0.99$, $n_{TA} = 0.98$, respectively, which leads to the conclusion that the in-plane acoustic phonon modes contribute dominantly to the heat capacity.

Moreover, considering the in-plane anisotropic nature of the b-P, b-As, and b-AsP structures, one expects an anisotropic contribution of LA and TA branches to the thermal properties. To examine this, we also calculate the direction-decomposed heat capacity of b-P, b-As, and b-AsP at low temperatures, which is presented in Fig 2(b). For the considered directions, Γ -X and Γ -Y, it is shown that the heat capacity along the Γ -X direction deviates from the total curve (solid) to the higher energy and has a linear temperature dependence. On the other hand, the heat capacity curves along the Γ -Y direction (acoustic phonon along the ZZ direction) display a behavior similar to the total curves for all single layers, indicating a dominant contribution to the low-temperature thermal behavior.

IV. ELECTRONIC AND OPTICAL PROPERTIES

In Figs. 3(a), 3(b) and 3(c), the electronic band structures of single-layer b-As, b-P, and b-AsP are presented. It is confirmed that single-layer b-As (b-P) is an indirect (direct) band gap semiconductor. The valence band maximum (VBM) and the conduction band minimum (CBM) are found to reside at the X - Γ / Γ and Γ / Γ high-symmetry points for b-As and b-P, respectively. The indirect (direct) energy band gaps for single layers of b-As (b-P) are calculated to be 1.29 (1.55) eV. The Janus single-layer b-AsP is a direct band gap semiconductor

with a band gap of 1.49 eV, which is close to that of b-P. As reflected by the atomic projections of the band structure shown in Fig. 3(c), both atoms contribute to the VBM and CBM in the Janus structure. However, the direct band gap nature of the Janus structure is found to arise from the surface-induced uniaxial strains on the As and P surfaces. Our analysis of the atomic orbital projections to the valence band edges at the X - Γ and Γ points reveals that in single layers of b-As and b-P these band edges are dominated by the (p_x-p_y) and (p_z) atomic orbitals, respectively. Therefore, the surface-induced in-plane uniaxial strains in the Janus crystal affect the valence band edges at the X - Γ point, which becomes energetically less favorable and results in the direct band gap behavior.

We also investigate the optical properties of all three single layers by obtaining the frequency-dependent dielectric function including the exciton states. In Fig. 4, we show the imaginary parts of the frequency-dependent dielectric function $\epsilon(\omega)$ for the AC and ZZ orientations. We also plot the oscillator strength as a bar under the respective exciton peak, which allows us to distinguish the individual excitonic states contributing to the spectrum. Each single-layer spectrum is dominated by a lowest-energy peak due to the exciton. From those peak positions, it is deduced that b-As, b-P, and b-AsP have optical band gaps of 1.11, 1.30, and 1.19 eV, respectively. Notably, b-As has an indirect electronic band gap which hinders the optical activity, in contrast to the direct band gap of Janus b-AsP. According to our results, by single-side substitutional doping of P atoms in single b-As, the optical activity can be increased at a slightly lower energy regime compared to that of single-layer b-P. Remarkably, all three single layers possess significant in-plane absorption anisotropy due to their puckered lattice structure. The spectra of the ZZ direction are shifted by ~ 0.6 eV through the higher energy for each single layer with significantly lower peak intensity compared to AC spectra.

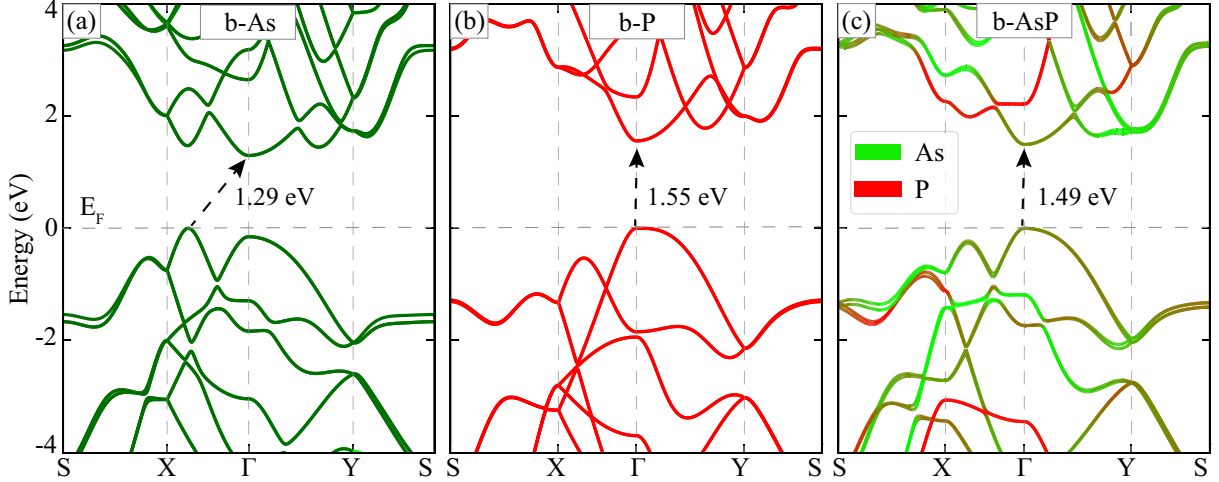


FIG. 3. The electronic band dispersions for single layers of (a) b-As, (b) b-P, and (c) Janus b-AsP. Here, red and green curves represent the contributions of As and P atoms to the electronic bands. The Fermi level is set to zero.

V. TIGHT-BINDING MODEL

Based on the large interest in the field of two-dimensional materials, a tight-binding model helps researchers who are interested in transport and electronic properties of finite systems using the Green's function theory and TB method. With the linear combination of atomic orbitals method a system can be described by a set of noninteracting single particles. Slater and Koster (SK) [38] showed that it is possible to reproduce the first-principles band structure using a set of integrals defined between different orbitals of neighbor atoms. SK scheme can be applied to construct the TB Hamiltonian of different systems in both orthogonal and nonorthogonal bases. To find a good fit to the first-principles data, one needs to follow a nonlinear fitting approach. In this work, we use the Levenberg-Marquardt method to find the independent parameters for both Hamiltonian. The idea is to find the SK

coefficients for the bonds defined in Fig. 5(a) as R_m , $m = 1, 2, \dots, 7$, to reproduce the band gap found from the HSE06 method.

For the lattice with a basis of four atoms, we assume a basis of four cubic harmonic orbitals [39] (one atomiclike s and three p_x , p_y , and p_z orbitals per atom). In the fitting procedure, we have many bands, and we should focus on regenerating the gap. To construct the TB model we need to solve the Schrodinger equation, which is a generalized eigenvalue problem, as follows:

$$\sum_{v'} \sum_{m'} [H_{mv, m'v'} - \epsilon_k S_{mv, m'v'}] c_{m'v'}(k) = 0, \quad (1)$$

in which H and S are the mono-electronic Hamiltonian and overlap matrix for the system. The elements of the matrices may be written as the following expression [40]:

$$H_{mv, m'v'} = \langle \phi_v(\mathbf{r} - \mathbf{r}_m) | H | \phi_{v'}(\mathbf{r} - \mathbf{r}_{m'}) \rangle, \quad (2)$$

$$S_{mv, m'v'} = \langle \phi_v(\mathbf{r} - \mathbf{r}_m) | \phi_{v'}(\mathbf{r} - \mathbf{r}_{m'}) \rangle, \quad (3)$$

in which the integrals are calculated over the whole unit cell and m and v run over the atoms in the unit cell and their orbitals s , p_x , p_y , and p_z , respectively.

Practically, the interatomic matrix elements, i.e., Eq. (2), cannot be calculated directly from the unknown wave functions. The expectation values of the Hamiltonian, represented by Slater and Koster [38], in the basis of the directed orbitals are presented in terms of eight integrals ($v_{ss\sigma}$, $v_{sp\sigma}$, $v_{pp\sigma}$, $v_{pp\pi}$, $s_{ss\sigma}$, $s_{sp\sigma}$, $s_{pp\sigma}$, $s_{pp\pi}$) as follows:

$$\langle s | H | s \rangle = v_{ss\sigma},$$

$$\langle s | H | p_i \rangle = n_i v_{sp\sigma},$$

$$\langle p_i | H | p_j \rangle = (\delta_{ij} - n_i n_j) v_{pp\pi} + n_i n_j v_{pp\sigma},$$

where \mathbf{r} is the vector along the bond, i runs over x , y , and z , and $n_i = \mathbf{r} \cdot \mathbf{e}_i / |\mathbf{r}|$ are the directional cosines. It should be noted that, to evaluate conjugate transpose matrices, one needs the rule of the angular quantum number: $\langle l | H | l' \rangle = (-1)^{l+l'} \langle l' | H | l \rangle$. In practice, the independent parameters are

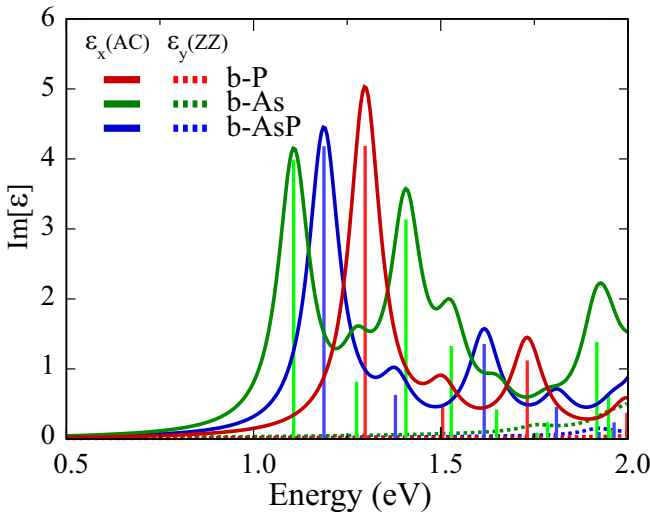


FIG. 4. For single layers of b-As, b-P, and b-AsP, the imaginary-part-dependent dielectric function along the AC (solid) and ZZ (dashed) directions.

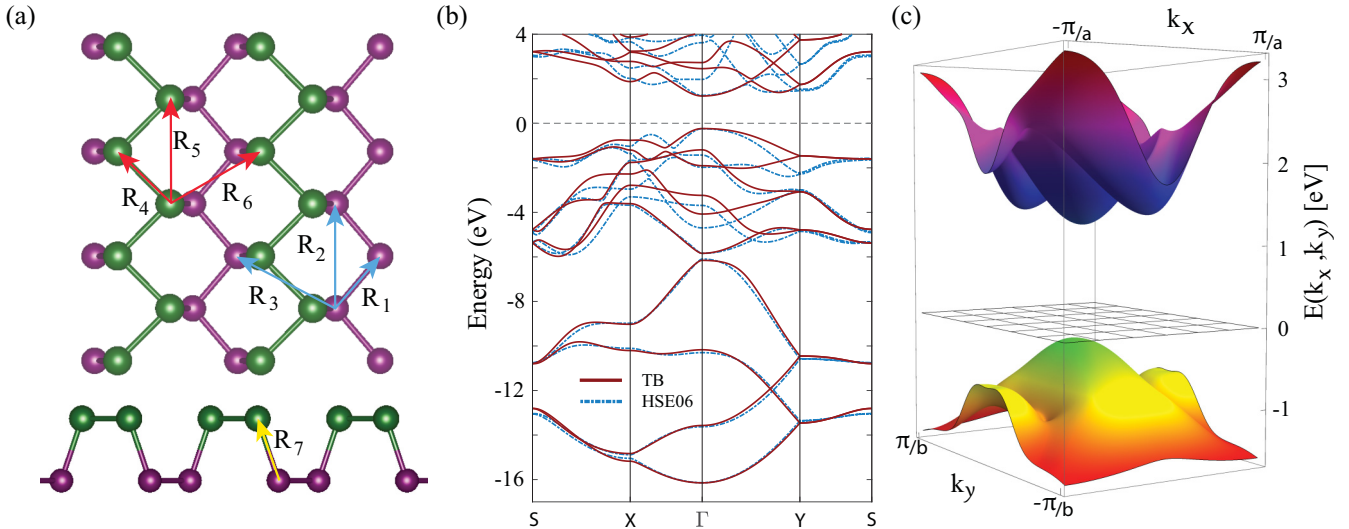


FIG. 5. (a) The vectors show the different bonds defined in our TB model. The blue and red vectors denote the interlayer bonds between P and As atoms, and the yellow vector indicates the intralayer bond. (b) The red curves are the TB band structures which are compared to that of the *ab initio* HSE06 results. (c) Three-dimensional plot of the valence and conduction bands of the TB model.

determined by fitting the energy bands that are obtained by *ab initio* methods.

In Table II, the Slater-Koster parameters of the system are presented for each R_m (see Fig. 5) as obtained by fitting the HSE06 energy bands. The on-site parameters of P and As atoms are also presented in Table III. Figure 5(b) shows a comparison of the band structure of the TB model and HSE06 method. A three-dimensional (3D) surface plot of the VBM and CBM as calculated from the TB model is shown in Fig. 5(c).

VI. ORIENTATION DEPENDENCE OF LINEAR ELASTICITY

The elastic properties of ultrathin 2D materials can be represented by two independent constants: the in-plane stiffness C , which is a measure of the rigidity of a material, and the Poisson ratio ν , which is the ratio of the transverse contraction strain to the longitudinal extension. In order to determine the linear-elastic constants, the elastic strain tensor elements C_{ij} are calculated, and the corresponding C and ν values are obtained for all directions of the lattice.

TABLE II. The Slater-Koster parameters for AsP structure (in eV).

R	$V_{ss\sigma}$	$V_{sp\sigma}$	$V_{pp\sigma}$	$V_{pp\pi}$
R_1	-2.114	-4.053	3.607	-1.442
R_2	0.169	0.251	-0.500	-0.010
R_3	-0.503	-0.352	0.160	-0.138
R_4	-1.219	-2.587	3.107	-0.570
R_5	-0.249	-0.084	0.739	-0.131
R_6	-0.046	-0.337	1.280	-0.249
R_7	1.839	1.226	-3.133	1.017

In order to obtain the anisotropy in the elastic constants, we fit $C(\theta)$ and $\nu(\theta)$ to the following functions [41,42]:

$$C(\theta) = \frac{(C_{11}C_{22} - C_{12}^2)}{C_{22}\cos^4(\theta) + A\cos^2(\theta)\sin^2(\theta) + C_{11}\sin^4(\theta)}, \quad (4)$$

$$\nu(\theta) = \frac{C_{12}\cos^4(\theta) - B\cos^2(\theta)\sin^2(\theta) + C_{12}\sin^4(\theta)}{C_{22}\cos^4(\theta) + A\cos^2(\theta)\sin^2(\theta) + C_{11}\sin^4(\theta)}, \quad (5)$$

where $A = (C_{11}C_{22} - C_{12}^2)/C_{66} - 2C_{12}$ and $B = C_{11} + C_{22} - (C_{11}C_{22} - C_{12}^2)/C_{66}$.

The in-plane stiffness [Fig. 6(b)] and Poisson ratio [Fig. 6(c)] display strong in-plane anisotropy between the ZZ and AC directions in single-layer Janus b-AsP because of the orthorhombic structure of the crystal, which exhibits four linear elastic constants, namely, C_{11} , C_{12} , C_{21} , and C_{22} . Note that the elastic constants of single-layer b-As and b-P are also calculated for comparison. As listed in Table IV, the in-plane stiffness of Janus b-AsP is calculated to be 22 and 70 N/m along the AC and ZZ directions, respectively. Such significant, although somewhat smaller, anisotropy is also found in single layers of b-As (20 and 55 N/m) and in b-P (30 and 92 N/m). It is evident that the response of the Janus b-AsP to applied strain along the AC direction is going to be much smaller because under applied strain the bonds between zigzag As and P chains get larger. Because there is no net charge transfer between these chains, the charges are mostly localized inside the chains. However, in the ZZ direction application of strain stretches the bond between As-As and P-P atoms, and thus, the structure displays more resistance to applied strain along

TABLE III. The on-site energies for As and P atoms (in eV).

	s	p_x	p_y	p_z
As	-10.446	-0.756	-0.346	-0.760
P	-8.047	1.537	1.116	-2.724

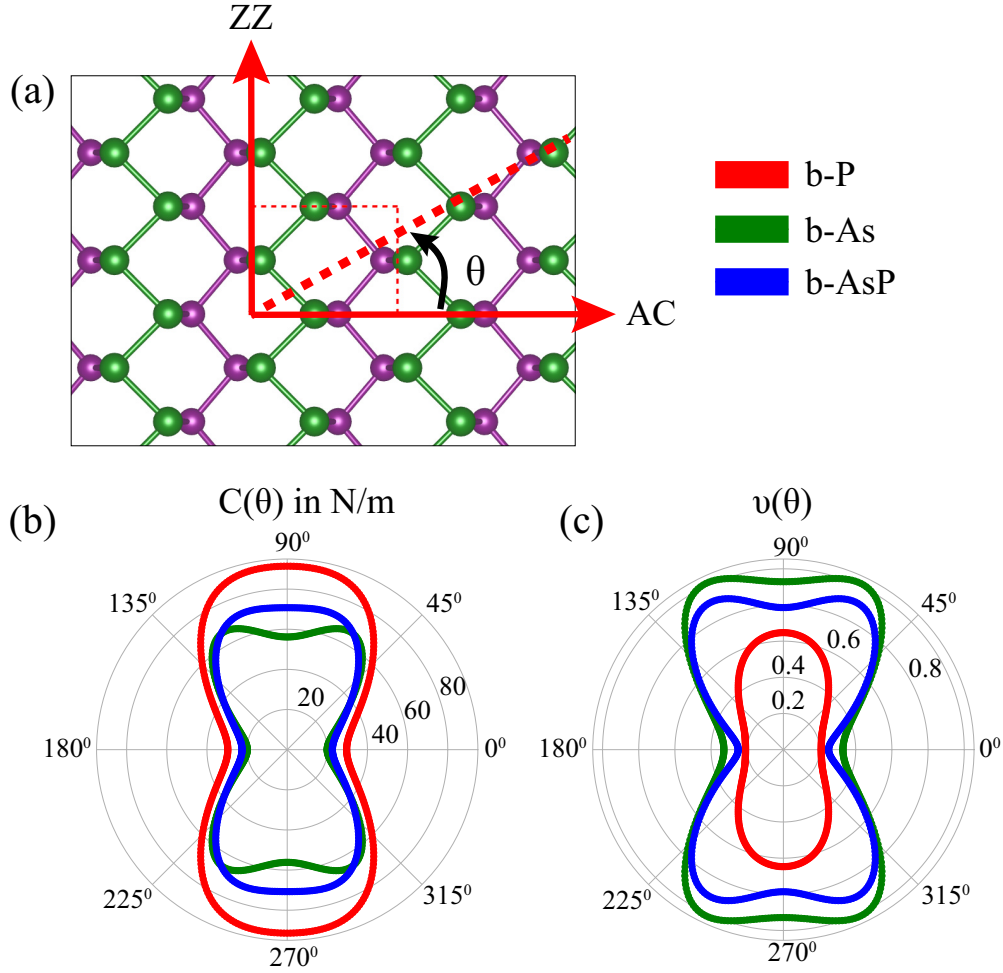


FIG. 6. (a) Schematic representation of the orientation angle θ . (b) The angle-dependent in-plane stiffness and (c) that of Poisson ratio.

the ZZ direction. In addition, for the strain angles around 90° (corresponding to the ZZ direction), the Janus b-AsP is found to possess less anisotropy than b-As. This is similar to the case of b-P, where the behavior of C is dominated by the P-P bonding states along the ZZ direction.

We further analyze the Poisson ratio of Janus b-AsP with respect to the lattice direction and compare it with that of b-As and b-P. The Poisson ratio is calculated to be 0.25 and 0.80 along the AC and ZZ directions, respectively. Notice that the Poisson ratio along the ZZ direction is extremely large compared to other 2D materials, which indicates the strong ability of Janus b-AsP to preserve its equilibrium state under external applied strain in the ZZ direction. In addition, the

anisotropy in the Poisson ratio around 0° (corresponding to the AC direction) increases in Janus b-AsP due to the bonded As and P chains.

VII. CONCLUDING REMARKS

In this study, by using DFT calculations, we predicted a dynamically stable puckered Janus single-layer b-AsP, which is composed of two different atomic sublayers, arsenic and phosphorus atoms. The calculated phonon spectrum revealed that Janus single-layer b-AsP is dynamically stable with either pure or coupled optical phonon branches arising from As and P atoms. The calculated Raman spectrum indicated that due to the relatively strong P-P bonds, As atoms have no contribution to the high-frequency optical vibrations. In addition, the orientation-dependent isovolume heat capacity reveals anisotropic contributions of LA and TA phonon branches to the low-temperature thermal properties.

Unlike its pristine counterparts, i.e., single layers of b-As and b-P, Janus single-layer b-AsP was shown to exhibit additional out-of-plane asymmetry having important consequences for the electronic, optical, and elastic properties. The electronic band structure calculations indicated the direct band gap nature of the Janus b-AsP, which is different from

TABLE IV. For single layers of b-As, b-P, and b-AsP, the relaxed-elastic coefficients C_{ij} , the corresponding in-plane stiffness C , and Poisson ratio ν , along AC and ZZ orientations.

Crystal	C_{11}	C_{22}	C_{12}	C_{AC}	C_{ZZ}	ν_{AC}	ν_{ZZ}
b-As	28	79	26	20	55	0.33	0.91
b-P	34	105	22	30	92	0.21	0.64
b-AsP	28	88	22	22	70	0.25	0.80

the indirect band gap of single-layer b-As. Moreover, the real and imaginary parts of the dynamical dielectric function including excitonic effects revealed a significant optical dichroism in Janus single-layer b-AsP. We further constructed a TB model for single-layer b-AsP which is expected to be useful for studying, e.g., transport properties of finite-size structures based on this Janus single-layer when combined with the Green's function approach. Furthermore, we investigated the linear-elastic properties of Janus single-layer b-AsP in terms of in-plane stiffness and the Poisson ratio with respect to the lattice orientation. We found that Janus single-layer b-AsP exhibits strong in-plane anisotropy in its Poisson ratio compared to single-layer b-P.

In conclusion, we predicted a dynamically stable puckered Janus single-layer b-AsP, and our results showed that this Janus single layer can distinctively be distinguished from its pristine counterparts (i.e., single-layers of b-As and b-P) by their different electronic, optical, thermal, vibrational, and elastic properties. The strong anisotropy of Janus single-layer b-AsP shown by its optical and elastic properties suggests that this 2D material is relevant for promising applications in optical dichroism and anisotropic nanoelasticity.

VIII. DATA AVAILABILITY

The supporting information for the tight-binding model and its results are available within the Supplemental Material [43] and TBSTUDIO software developed based on the Slater-Koster method. The explicit form of the Tight-binding Hamiltonian and the overlap matrices are given as supporting information. The software has been made available [44]. The results for b-AsP are accessible in the example folder of TBSTUDIO. The supporting codes in additional programming languages, i.e., MATLAB, MATHEMATICA, PYTHON, C, C++, and FORTRAN, are also accessible through code generator tools in TBSTUDIO.

ACKNOWLEDGMENTS

This work was supported by the German Science Foundation (DFG) within SFB/TRR80 (project G3) and the FLAG-ERA project TRANS-2D-TMD. M.Y. was supported by a postdoctoral fellowship from the Flemish Science Foundation (FWO-VI). Computational resources were provided by the Flemish Supercomputer Center (VSC) and Leibniz Supercomputer Centrum (project pr87ro).

-
- [1] S. K. Novoselov, A. Mishchenko, A. Carvalho, and A. H. C. Neto, *Science* **353**, aac9439 (2016).
- [2] K. S. Novoselov, A. K. Geim, S. V. Morozov, D. Jiang, M. I. Katsnelson, I. V. Grigorieva, S. V. Dubonos, and A. A. Firsov, *Nature (London)* **438**, 197 (2005).
- [3] A. H. Castro Neto, F. Guinea, N. M. R. Peres, K. S. Novoselov, and A. K. Geim, *Rev. Mod. Phys.* **81**, 109 (2009).
- [4] P. Vogt, P. De Padova, C. Quaresima, J. Avila, E. Frantzeskakis, M. C. Asensio, A. Resta, B. Ealet, and G. Le Lay, *Phys. Rev. Lett.* **108**, 155501 (2012).
- [5] M. E. Davila, L. Xian, S. Cahangirov, A. Rubio, and G. Le Lay, *New J. Phys.* **16**, 095002 (2014).
- [6] F. F. Zhu, W. J. Chen, Y. Xu, C. L. Gao, D. D. Guan, C. H. Liu, D. Quian, S. C. Zhang, and J. F. Jia, *Nat. Mater.* **14**, 1020 (2015).
- [7] Q. H. Wang, K. Kalantar-Zadeh, A. Kis, J. N. Coleman, and M. S. Strano, *Nat. Nanotechnol.* **7**, 699 (2012).
- [8] X. Xu, W. Yao, D. Xiao, and T. F. Heinz, *Nat. Phys.* **10**, 343 (2014).
- [9] A. Bafekry, B. Mortazavi, and S. Farjami Shayesteh, *J. Magn. Magn. Mater.* **491**, 165565 (2019).
- [10] A. Bafekry, M. Ghergherehchi, and S. Farjami Shayesteh, *Phys. Chem. Chem. Phys.* **21**, 10552 (2019).
- [11] A. Bafekry, C. Stampfl, and F. M. Peeters, *Sci. Rep.* **10**, 213 (2020).
- [12] H. Lui, A. T. Neal, Z. Zhu, Z. Luo, X. Xu, D. Tomanek, and P. D. Ye, *ACS Nano* **8**, 4033 (2014).
- [13] J. Qiao, X. Kong, Z. X. Hu, F. Yang, and W. Ji, *Nat. Commun.* **5**, 4475 (2014).
- [14] V. Tran, R. Soklaski, Y. Liang, and L. Yang, *Phys. Rev. B* **89**, 235319 (2014).
- [15] D. Çakır, C. Sevik, and F. M. Peeters, *Phys. Rev. B* **92**, 165406 (2015).
- [16] S. Yuan, A. N. Rudenko, and M. I. Katsnelson, *Phys. Rev. B* **91**, 115436 (2015).
- [17] L. L. Li, B. Partoens, W. Xu, and F. M. Peeters, *2D Mater.* **6**, 015032 (2018).
- [18] Y. Chen, C. Chen, R. Kealhofer, H. Lu, Z. Yuan, L. Jiang, J. Suh, J. Park, C. Ko, H. S. Choe, J. Avila, M. Zhong, and Z. Wei, *Adv. Mater.* **30**, 1800754 (2018).
- [19] A. Kandemir, F. Iyikanat, and H. Sahin, *J. Mater. Chem. C* **7**, 1228 (2019).
- [20] B. Akgenc, *J. Mater. Sci.* **54**, 9543 (2019).
- [21] A.-Y. Lu, H. Zhu, J. Xiao, C.-P. Chuu, Y. Han, M.-H. Chiu, C.-C. Cheng, C.-W. Yang, K.-H. Wei, Y. Yang, Y. Wang, D. Sokaras, D. Nordlund, P. Yang, D. A. Muller, M.-Y. Chou, X. Zhang, and L.-J. Li, *Nat. Nanotechnol.* **12**, 744 (2017).
- [22] J. Zhang, S. Jia, I. Kholmanov, L. Dong, D. Er, W. Chen, H. Guo, Z. Jin, V. B. Shenoy, L. Shi, and J. Lou, *ACS Nano* **11**, 8192 (2017).
- [23] L. Dong, J. Lou, and V. B. Shenoy, *ACS Nano* **11**, 8242 (2017).
- [24] A. Kandemir and H. Sahin, *Phys. Rev. B* **97**, 155410 (2018).
- [25] M. Yagmurcukardes, C. Sevik, and F. M. Peeters, *Phys. Rev. B* **100**, 045415 (2019).
- [26] B. Liu, M. Kopf, A. N. Abbas, X. Wang, Q. Guo, Y. Jia, F. Xia, R. Weihrich, F. Bachhuber, F. Pielhofer, H. Wang, R. Dhall, S. B. Cronin, M. Ge, X. Fang, T. Nilges, and C. Zhou, *Adv. Mater.* **27**, 4423 (2015).
- [27] M. Amani, E. Regan, J. Bullock, G. H. Ahn, and A. Javey, *ACS Nano* **11**, 11724 (2017).
- [28] E. P. Young, J. Park, T. Bai, C. Choi, R. H. DeBlock, M. Lange, S. Poust, J. Tice, C. Cheung, B. S. Dunn, M. S. Goorsky, V. Ozolins, D. C. Streit, and V. Gambin, *ACS Appl. Nano Mater.* **1**, 4737 (2017).
- [29] I. Ozdemir, D. Ozaydin, H. A. Olgar, and E. Akturk, *Mater. Res. Exp.* **6**, 065032 (2019).

- [30] G. Kresse and J. Furthmüller, *Phys. Rev. B* **54**, 11169 (1996).
- [31] J. P. Perdew, K. Burke, and M. Ernzerhof, *Phys. Rev. Lett.* **77**, 3865 (1996).
- [32] J. Heyd, G. E. Scuseria, and M. Ernzerhof, *J. Chem. Phys.* **118**, 8207 (2003).
- [33] D. Alfe, *Comput. Phys. Commun.* **180**, 2622 (2009).
- [34] M. Yagmurcukardes, F. M. Peeters, and H. Sahin, *Phys. Rev. B* **98**, 085431 (2018).
- [35] M. Yagmurcukardes, C. Bacaksiz, E. Unsal, B. Akbali, R. T. Senger, and H. Sahin, *Phys. Rev. B* **97**, 115427 (2018).
- [36] A. A. Balandin, *Nat. Mater.* **10**, 569 (2011).
- [37] H. Sahin, *Phys. Rev. B* **92**, 085421 (2015).
- [38] J. C. Slater and G. F. Koster, *Phys. Rev.* **94**, 1498 (1954).
- [39] T. Kwiatkowski, S. Olszewski, and A. Wierzbicki, *Int. J. Quantum Chem.* **11**, 21 (1977).
- [40] W. C. Lu, C. Z. Wang, K. Ruedenberg, and K. M. Ho, *Phys. Rev. B* **72**, 205123 (2005).
- [41] Y. Ma, L. Kou, B. Huang, Y. Dai, and T. Heine, *Phys. Rev. B* **98**, 085420 (2018).
- [42] E. Cadelano, P. L. Palla, S. Giordano, and L. Colombo, *Phys. Rev. B* **82**, 235414 (2010).
- [43] See Supplemental Material at <http://link.aps.org/supplemental/10.1103/PhysRevB.101.134102> for more details.
- [44] TBSTUDIO, <https://tight-binding.com>.